

# Separation of simultaneous source blended data using radially and source similarity attributes

*Joseph Jennings and Shuki Ronen*

## ABSTRACT

Deblending data from simultaneous sources is an underdetermined problem. This problem cannot be solved based on fitting blended data to unknown deblended data without more assumptions. Useful such assumptions are, for example, that the deblended data are continuous in common receiver gathers, or that both blended and deblended data fit one earth reflectivity model. We point to the opportunity to use multi-component data and different sources in addition to such assumptions. We developed a method that assigns a probability to the existence of simultaneous source interference indicating the likelihood that at certain times, the interference originated from another active source. To estimate this probability we compute two attributes which we call radially and source-signature similarity. Radially is calculated for multi-component data with horizontal components such as ocean bottom seismometers or multi-sensor streamers. Source signature similarity is useful when sources have different source signatures. The end goal of this work is to use this probability as additional information in deblending and imaging simultaneous source data.

## INTRODUCTION

To reduce acquisition time of seismic surveys, and therefore high acquisition costs, geophysicists have proposed reducing the wait time between shots (Beasley et al., 1998) and to sustain seismic interference (Lynn et al., 1987). In land surveys, in which it is possible to encode the different shots using vibroseis technology, and also in which there exists a much higher tolerance for random noise, this reduction in wait time, known as simultaneous source acquisition or blending, is common (Abma et al., 2012; Womack et al., 1990). In marine surveys, where there exists a much higher expectation for data quality and vibroseis is not yet feasible, simultaneous source acquisition is still very much a research topic in spite of the fact that many production surveys have been done (Abma et al., 2012).

For the separation of blended-marine seismic data, there have been a number of proposed algorithms, many of which result in high quality seismic images. These algorithms can be grouped into two different types. The first images these data as is, in their blended state (Tang et al., 2009). The problem with this approach is these methods are very much dependent on a velocity model and they also suffer from

significant cross-talk artifacts (Leader, 2015). The second type methods propose to separate the blended data and then image the data after separation.

The majority of the algorithms that “deblend” the data before imaging rely on the fact that with random time delays in the acquisition (shot intervals) the interference from the other shots will appear as random noise in the common-receiver, common-offset and common-midpoint domains (Huo et al., 2012). Under this assumption a variety of methods can be used that can be as simple as a stack to decrease the incoherent noise. More complicated filtering techniques have also been proposed to remove the interference as one would remove random noise (Chen, 2014). Another sub-class of these techniques that separate the data before imaging are known as inversion separation techniques (Abma and Yan, 2009). While most of these techniques are done in the data space, (Leader, 2015), proposed an image-space technique in which the data are separated in the extended image space and then inverse demigrated to obtain the deblended data. Regardless of the domain in which the sources are separated, all of these techniques attempt to solve an undetermined system of equations by inverting a blending operator (Berkhout, 2008). (Abma and Yan, 2009) point out that to successfully invert this operator and recover the unblended data, additional constraints are required. They propose the similarity of nearby shots as an additional constraint for separation. Other authors (Leader, 2015) have proposed additional constraints based on the fact that both blended data and unblended data are related to the same reflectivity model. In this report, we propose an additional constraint that relies on multi-component data and data acquired with more than one source signature. Herein, we define two attributes that we call radially and source signature similarity. We demonstrate the computation of these attributes on the multi-component ocean bottom node (OBN) data from the Forties Delta platform acquired by Apache North Sea Limited in the North Sea (Alves, 2015). In addition to the multiple components that enable us to compute our radiality attribute, these data have a varying source signature (Jennings and Ronen, 2015) which also allow us to compute the source signature similarity attribute.

The outline of this report is as follows: first, we introduce the acquisition geometry and data acquired by the Forties-Delta OBN array. Then, we perform a quality-check (QC) of the radial and transverse energy as well as the source signature present within these data. In doing this, we follow the approach of (Ronen et al., 2012) of applying normal (NMO) and hyperbolic-moveout (HMO) corrections and computing root-mean square (RMS) maps of the first arrival. We then introduce the radiality and similarity attributes and show results of computing these attributes on the Forties data. With these attributes, we can then assign probabilities over time windows in our data, where the probabilities indicate the likelihood that the interference in a give time window originated from another active source. Lastly, we present a toy optimization problem to show how these probabilities can be used as an additional constraint for simultaneous source deblending.

## NODE QUALITY CONTROL

As explained in (Alves, 2015), the Apache Forties oil field data were acquired as part of an ocean-bottom node survey with the goal of imaging gas clouds under producing oil rigs. It consisted of three platforms denoted as the Beta, Charlie and Delta platforms. The shot-receiver geometry for the Delta platform is shown in Figure 1(a). For this report, all the figures we show were performed with data from node 002 as indicated in Figure 1(b).

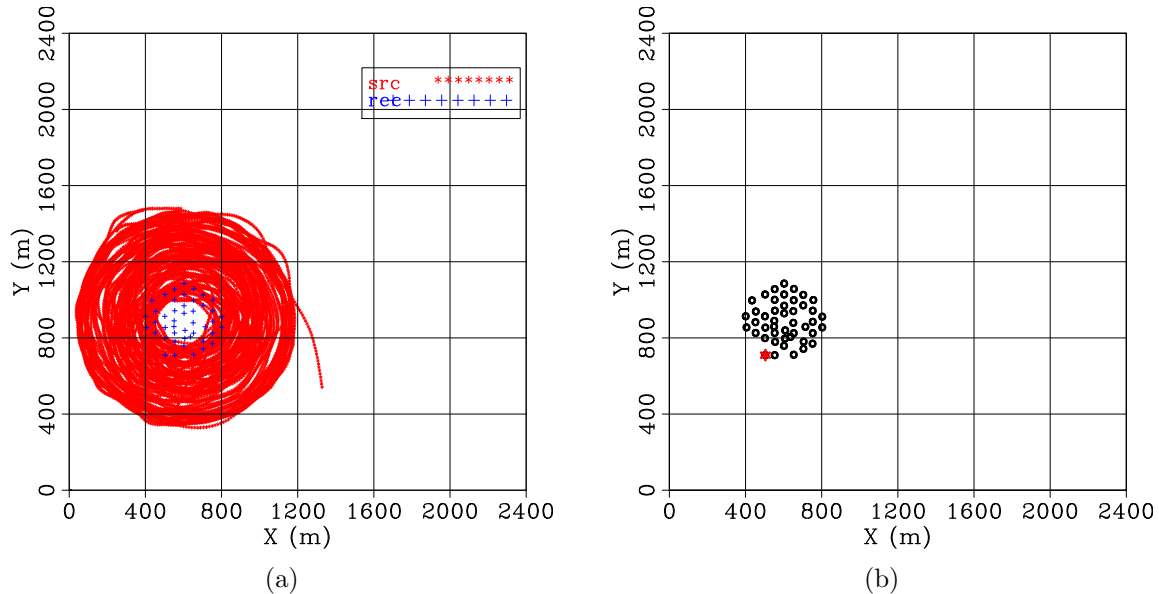


Figure 1: (a) The shot-receiver geometry for the Apache Forties survey around the Delta platform. The survey consisted of 14485 shots and 48 nodes. The source vessel circled around the platform in a spiral pattern and the receivers were arranged in an approximate hexagonal pattern around the platform with a 50 m node interval. (b) Node 002 is highlighted on the receiver map with the red star. This node was chosen for the minimal amount of instrument noise introduced in the data. [ER]

A selection of 250 shots are displayed in Figure 2. From left to right the hydrophone, vertical, radial and transverse components are displayed. In examining the different components of the data in this figure, it is clear that the majority of multi-component energy is radial while there does exist some energy on the second break as well as on the shear wave arrivals. Next, in hopes to see reflections as well as multiples in our data, we apply a NMO correction at water velocity. The results of the NMO are shown in Figure 3. With the data NMO corrected, we can clearly observe several reflections, multiples and as before the source signature and shear-wave arrivals.

We then applied a HMO to flatten the first arrival. This application allowed us to further distinguish the bubble period from the shear waves. The application of the HMO to the raw data is shown in Figure 4. In this figure, the source signature is flat but the shear waves still exhibit moveout. Figure 5 is a zoom-in of the results

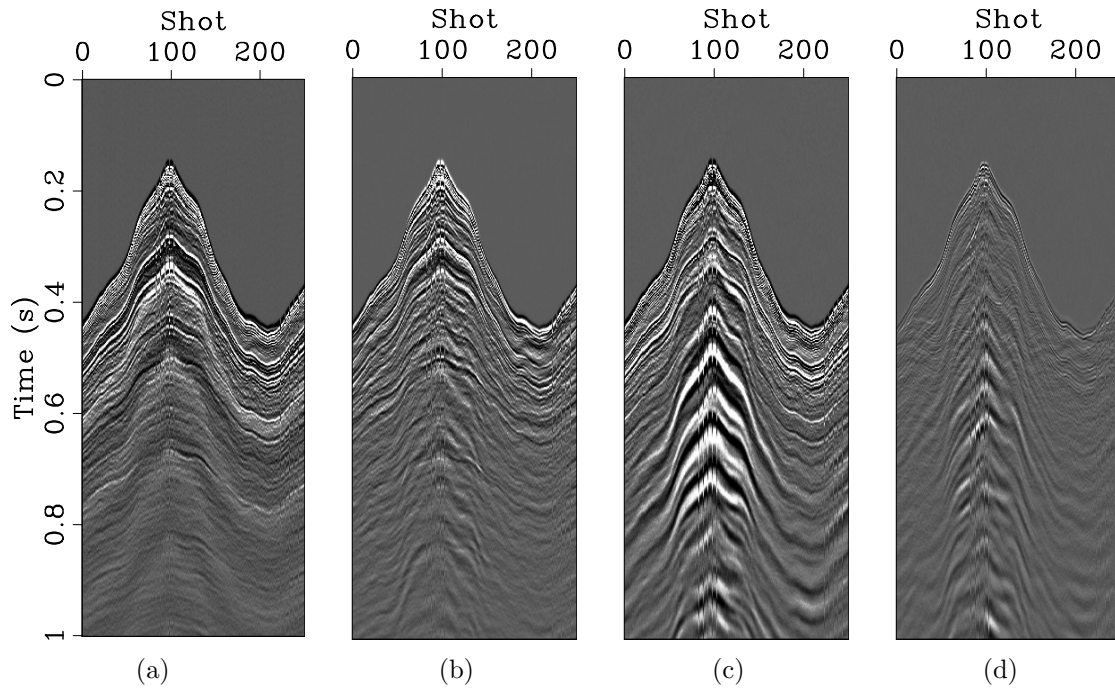


Figure 2: The raw data. The hydrophone component (a), vertical component (b), radial component (c) and transverse component (d). On the hydrophone component dipping periodic events due to the oscillating bubble are easily observed with a period of about 200 ms. The dipping periodic events on the radial and transverse components are due to measured shear wave arrivals (not to be confused with the bubble period). It is clear that measured radial energy is much larger than the measured transverse energy. [ER]

joseph1/. APAC-03-002-h-raw,APAC-03-002-v-raw,APAC-03-002-r-raw,APAC-03-002-t-raw

of HMO shown in Figure 4. In this figure, we can make two important observations. The first is that on each of the components except the transverse, the direct arrival is seen at about 0.1 s. On the transverse it appears a few milliseconds later. We also observe that there is some energy on the direct arrival measured on the transverse component. As this event and other energy originating from the water (e.g. water-bottom multiples) are purely radial (Gaiser et al., 1998), we should not expect to see any measured energy due to these arrivals on the transverse component. Our explanation for this unexpected energy is instrument noise (rattling of the cowling on the node). We call this delayed instrument noise the “second break”. Another reason for which there may exist more than usual energy on the transverse component is caused by inaccurate rotation. For the last step of our QC, we analyze the accuracies of the rotations applied to the data.

In Figure 6, we show the RMS of one second of each shot of the common-receiver gather for each component of the raw data. The location of the node is indicated by the star on the map. Observing Figures 6(c) and 6(d), we can see that the main energy lobes are not aligned directly north-south and east-west. This lack of alignment is most likely due to the inaccuracies of the tilt measurements taken by the node. This inaccuracy in the rotation is then propagated into the rotation of the radial and transverse components causing energy that is actually radial to be rotated into the transverse component.

In performing this QC, we have shown that there does exist energy on the transverse component where we did not expect. When computing the radially attribute, it is key that we understand from where the energy is coming on the radial and transverse components. As we will show in the coming sections, in order for our radially attribute to be useful in simultaneous source deblending, we desire minimal energy on the transverse component.

## METHODOLOGY

### Radiality

We define the radiality  $R$  of a seismic trace as follows:

$$R = \frac{E_{radial}}{E_{transverse}}, \quad (1)$$

where  $E$  is the energy of the trace computed by way of leaky integration ((Claerbout, 2014)). As we have shown that most of the energy is generally radial, especially for the early arrivals, then we can expect that the radiality will generally be large. Consider though, the case in which we have a simultaneous source survey as shown in Figure 7.

As the radial component of a multi-component trace is defined to point in the direction of the source-receiver azimuth then, for a single experiment with two sources,

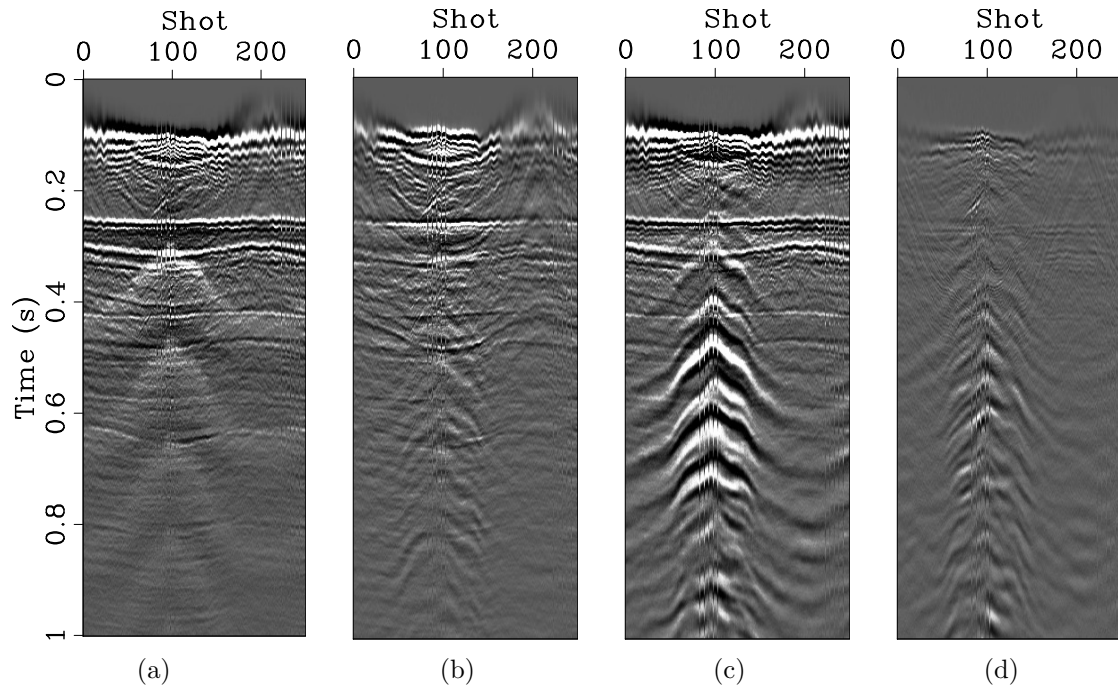


Figure 3: A NMO correction applied to the data shown in Figure 2. (a) Hydrophone component, (b) vertical component, (c) radial component, and (d) transverse component. Once again, we see a very pronounced source signature on the hydrophone component. On each of the components we observe the direct arrival at approximately 0.1 s and the first multiple (mirror image of the seabed) at approximately 0.25 s. As expected, these events are very weak on the transverse as they are purely radial. We also see measured shear waves with considerable moveout on the radial component beginning at about 0.4 s. [ER]

joseph1/. APAC-03-002-h-nmo,APAC-03-002-v-nmo,APAC-03-002-r-nmo,APAC-03-002-t-nmo

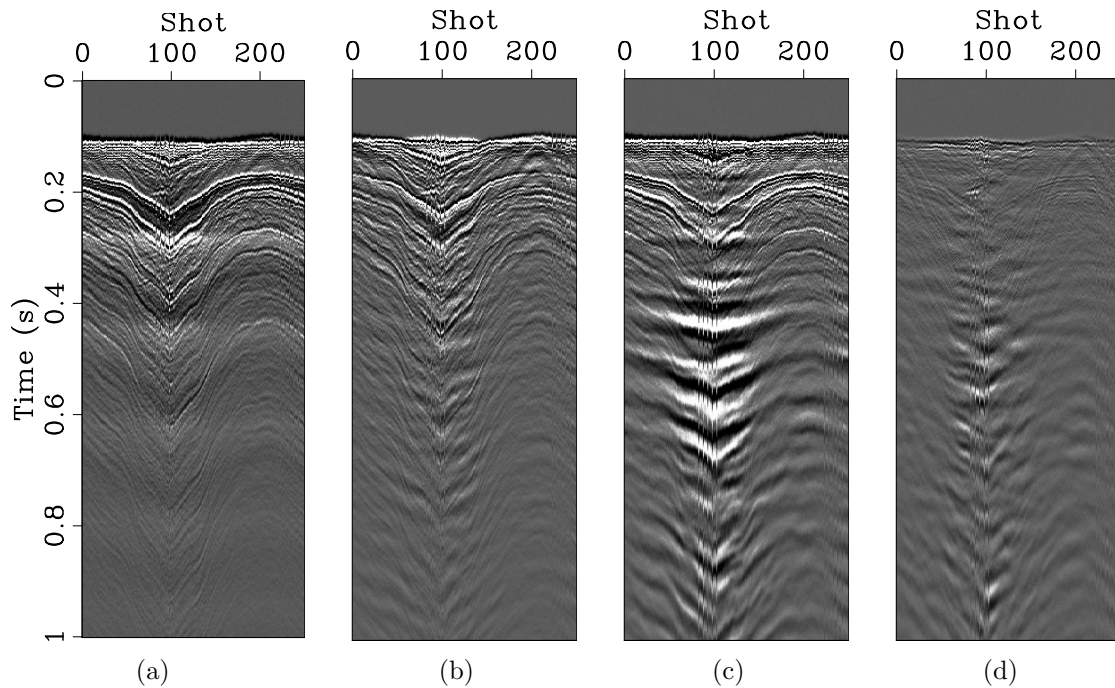


Figure 4: HMO applied to the data in Figure 2 in order to flatten the water bottom and distinguish the bubble period from the shear waves. (a) Hydrophone component, (b) vertical component, (c) radial component, and (d) transverse component. On the hydrophone component, we can clearly observe the bubble period of approximately 200 ms. On the radial component, we still observe moveout on the shear wave arrivals. [ER]

joseph1/. APAC-03-002-h-hmo,APAC-03-002-v-hmo,APAC-03-002-r-hmo,APAC-03-002-t-hmo

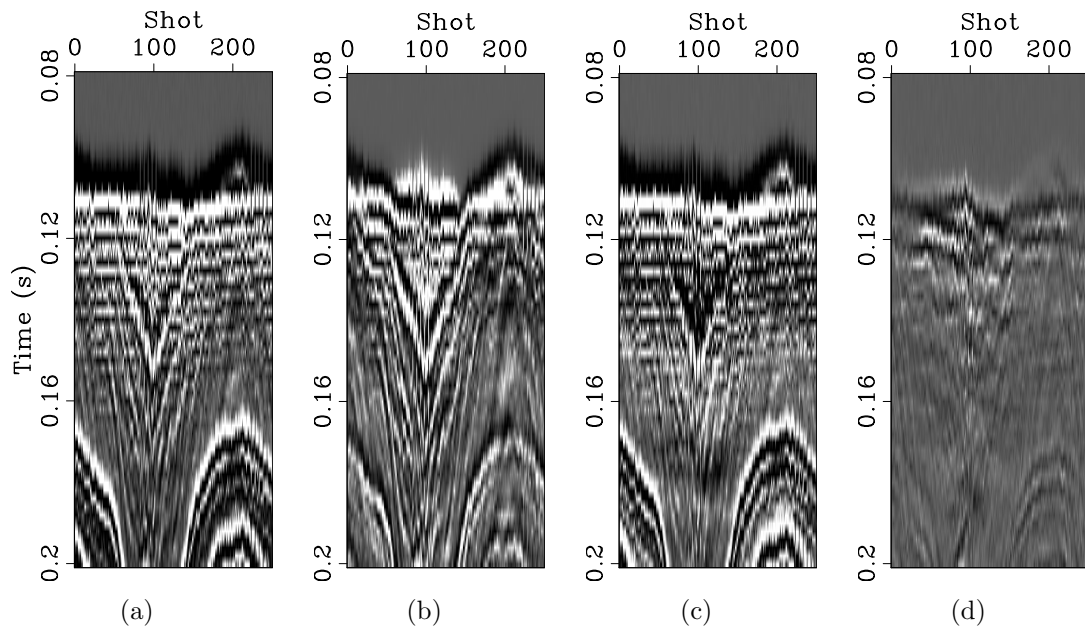


Figure 5: A zoom-in of the data in Figure 4 over a window of 80 to 200 ms. (a) Hydrophone component, (b) vertical component, (c) radial component, and (d) transverse component. Two important observations can be made observing the transverse component. The first is that the first arrival appears to come later than the first arrivals measured on the other components. The second is that the first arrival on the transverse clearly has non-zero energy. We believe this can be explained by the incident direct arrival that when it hits the node, causes the cowling of the node to rattle and therefore is recorded on the data. [ER]

joseph1/. 002-h-hmo-sm,002-v-hmo-sm,002-r-hmo-sm,002-t-hmo-sm

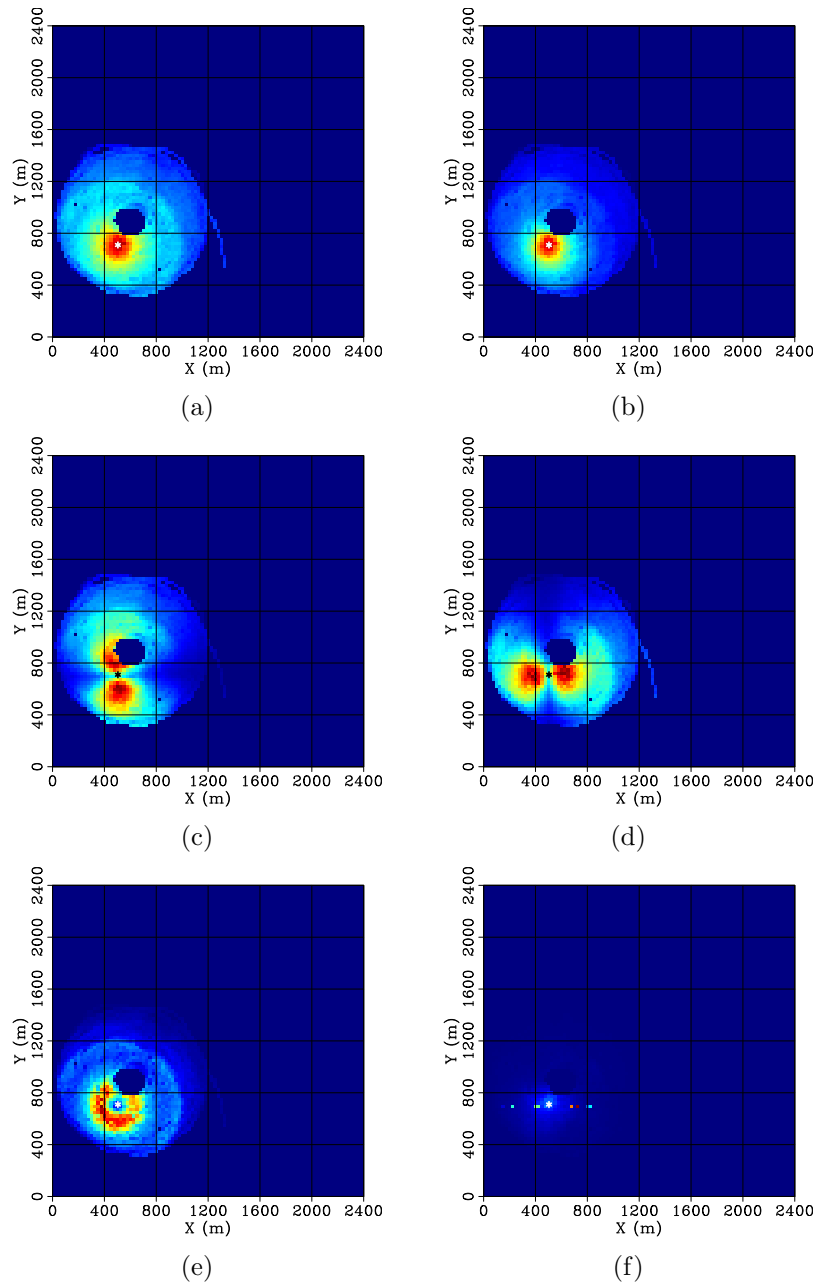


Figure 6: RMS of (a) hydrophone component, (b) vertical component, (c) north component, (d) east component, (e) radial component, and (f) transverse component. The star (white for all but panels (c) and (d)) located near the center of the energy on the maps indicates the location of the node. The main energy lobes on both the north and east components are clearly not aligned vertically and horizontally respectively, indicating errors in the rotation. The error is also clear on the radial component as we see that the node is not located exactly at the center of the ring of energy. As a result of this error, we can see more than expected energy on the transverse component map. Note that the change in color of the star was done only for display. [ER]

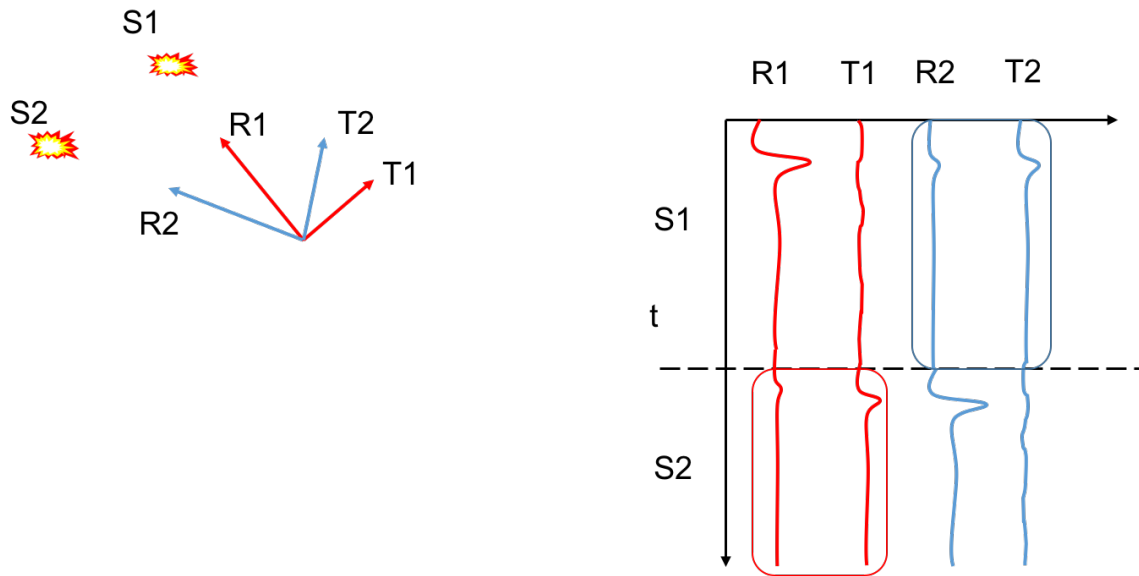


Figure 7: Diagram depicting the measured energy on the radial and transverse components in a simultaneous source survey. This survey consists of two sources and one multicomponent receiver which results in four traces as for each shot we rotate the data into the source receiver azimuth. First, source one fires and we observe a significant amount of radial energy measured on  $R1$  and very little energy on  $T1$ . On  $R2$  and  $T2$  we see that because  $T2$  is oriented more in the direction of  $R1$ , then it will record more energy from source one than will  $T1$  and  $R2$ . After source one fires, then source two emits a pulse. As was seen for source one, trace  $R2$  will record more energy than  $T2$  and  $T1$  will record more energy than  $R1$ . If we then compute the radiality over time windows for each of these traces we would see areas of low radiality in the circled areas shown over the recorded data. Thus we see that the radiality is low between  $R2$  and  $T2$  due to the recorded interference generated by source one. Likewise we see low radiality on traces  $R1$  and  $T1$  due to interference generated by source two. In this manner, radiality can serve as an indicator for simultaneous source interference. [NR]

four traces will be recorded (labeled  $R1$ ,  $T1$ ,  $R2$ , and  $T2$  in Figure 7). Observing both the transverse traces, we see that the transverse component acts as an indicator for the interference from the other source. In fact, if the sources are positioned such that  $R1$  and  $R2$  are orthogonal then, all the energy from source one will be recorded on  $T2$  and likewise for source two and  $T1$ . If we then compute the radially over time windows along these traces, we would find that the radially is low between  $R1$  and  $T1$  at later times and low between  $R2$  and  $T2$  at earlier times. This is indicated in the circled regions in Figure 7. Thus, radially can serve as indicator for simultaneous source interference. We can then use this indicator to assign a relative probability of the presence of simultaneous source interference over a time window.

As a sanity check, we show the radially of the unblended Forties data. To compute the radially, we first take the absolute value of trace; and then, apply a leaky integration. Doing this procedure gives us the energy. Then, dividing the energy of the radial  $E_{radial}$  by the energy of the transverse  $E_{transverse}$  gives us the radially. In Figure 8, we show the computed energy of the data shown in Figures 2(c) and 2(d). The resulting radially is shown in Figure 8(c). We then extract one trace from each of the gathers shown in Figure 8 and show the energy and radially in Figure 9. As expected, there is significantly greater amount of energy on the radial trace than there is on the transverse trace resulting in a large radially.

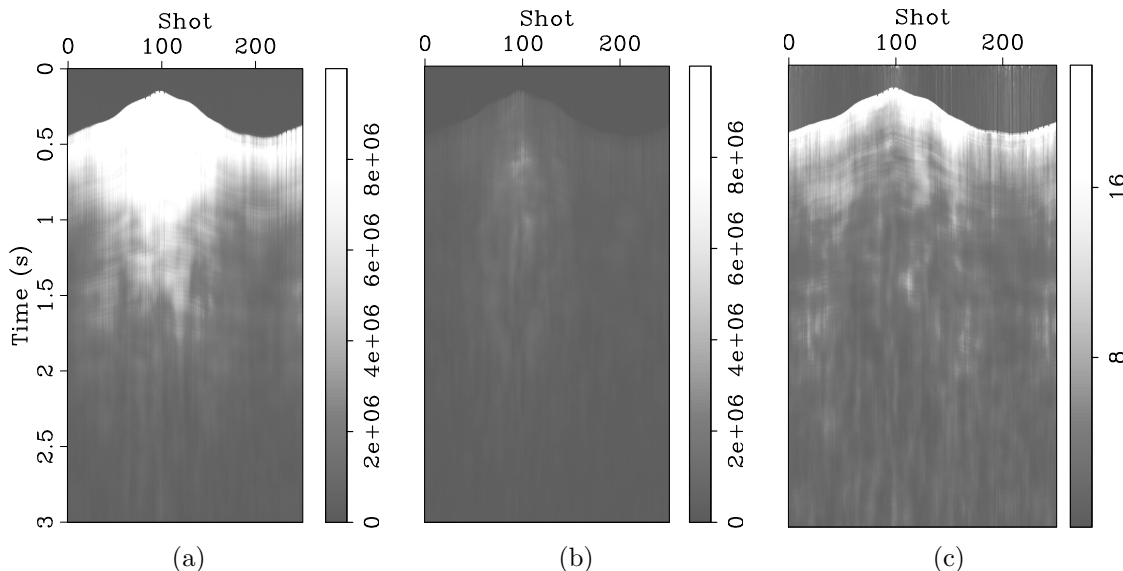


Figure 8: (a) The energy of the radial component computed by way of leaky integration. (b) The energy of the transverse component computed by way of leaky integration. (c) The radially ((a) divided by (b)). From the radially, we observe that most of the radial energy comes from the early-arrivals. [ER]

joseph1/. r-envlek-002, t-envlek-002, rad-lek-gat-002

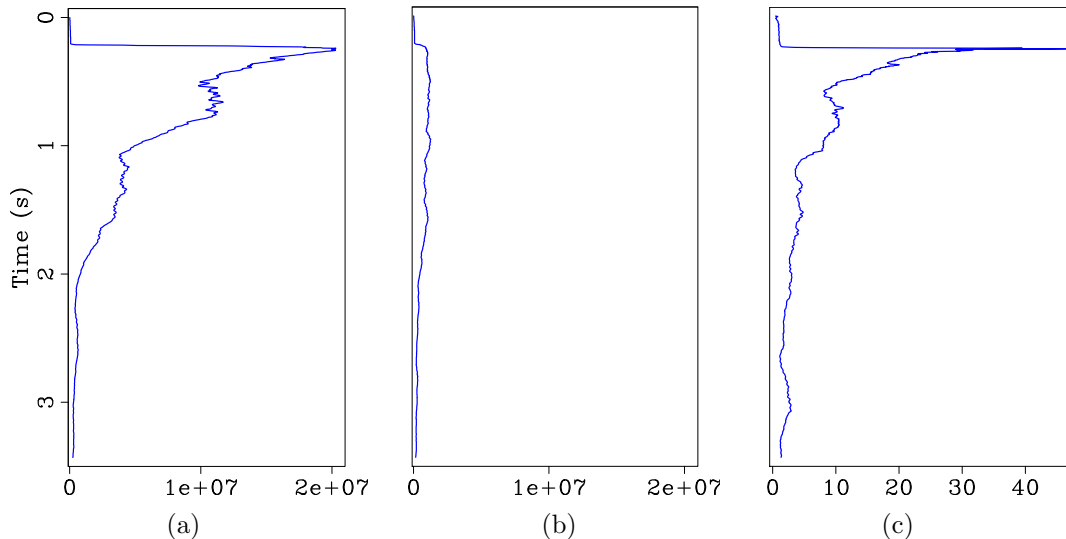


Figure 9: (a) Trace 175 extracted from the radial component energy gather (Figure 8(a)). (b) Trace 175 extracted from the transverse component energy gather (Figure 8(b)). (c) Trace 175 extracted from the radiality gather (Figure 8(c)) As expected, we observe large radiality for the early-arrivals and then the radiality slowly decreases with depth. [ER] `joseph1/. r-envleaky-002, t-envleaky-002, rad-Leaky-002`

## Similarity

In addition to radiality, we introduce another attribute that could aid current simultaneous source inversion schemes. This attribute we denote as similarity and define as follows:

$$S_{12} = \frac{\max(\mathbf{d}_1 \star \mathbf{d}_2)}{\sqrt{\max(\mathbf{d}_1 \star \mathbf{d}_1)\max(\mathbf{d}_2 \star \mathbf{d}_2)}}, \quad (2)$$

where  $S_{12}$  is the similarity between signals  $\mathbf{d}_1$  and  $\mathbf{d}_2$  and  $\star$  denotes the cross-correlation. Equation (2) is simply a normalized-cross correlation recognized as a basic algorithm for detecting waveforms in seismic data and similarly defined as coherency in (White, 1980). Figure 10 is a diagram that explains how this attribute can be used for detecting simultaneous source interference. It shows that by cross-correlating the different sources with the simultaneous source data, the similarity attribute will allow us to detect the presence of simultaneous source interference and also from which source the interference originated.

For operational reasons, the Forties-delta dataset were acquired with multiple source signatures. This unique acquisition creates an opportunity for us to test the similarity attribute on these data. The data and their spectra with an HMO applied are shown in Figure 11. In this figure, three zones are readily apparent in which the bubble period of the source signature has changed. In Figure 13(a) we show the positions of the shots for each of the zones. As the node lies in zone two, we can expect that source two will have the greatest energy.

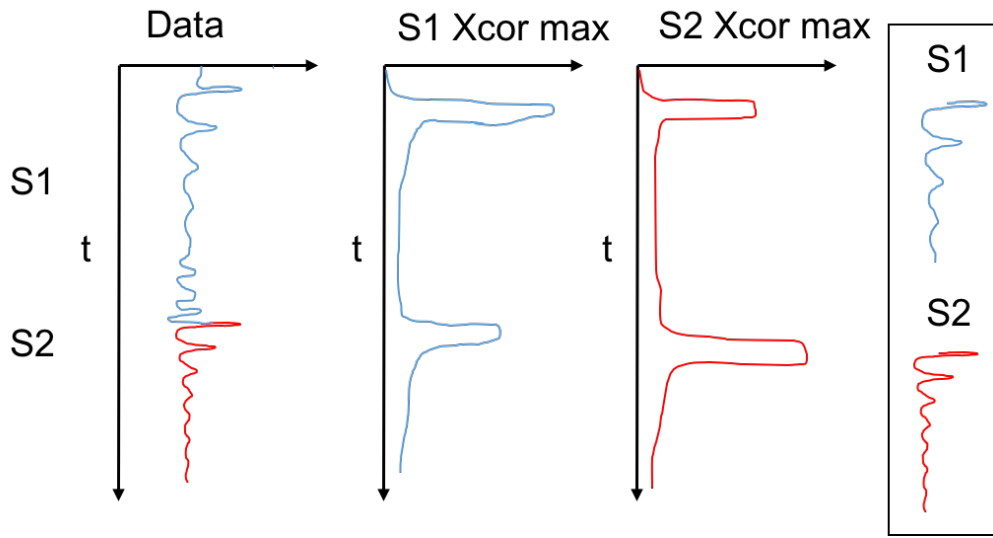


Figure 10: A diagram explaining how similarity can be used as an indicator for simultaneous source interference. The leftmost graph displays a data trace that was acquired in a simultaneous source survey where the sources had different signatures,  $S1$  and  $S2$ . These signatures are shown in the legend on the far right. If we compute the similarity between the data trace and  $S1$  over time windows, then we would obtain the middle graph. Notice in this plot that there are two peaks, one which corresponds maximum of the similarity between  $S1$  and itself, and the other which comes from the measured similarity between  $S1$  and  $S2$ . Likewise, we can compute the similarity between the data and  $S2$  which would result in the rightmost graph. Once again we observe two peaks that correspond to maxima of similarity with itself and the measured similarity between  $S2$  and  $S1$ . We see that the similarity attribute has detected more than one source signature on a single data trace. Moreover, it gave us the location of the source signature on the measured data. In this manner, source signature similarity can serve as an indicator for simultaneous source interference. [NR]

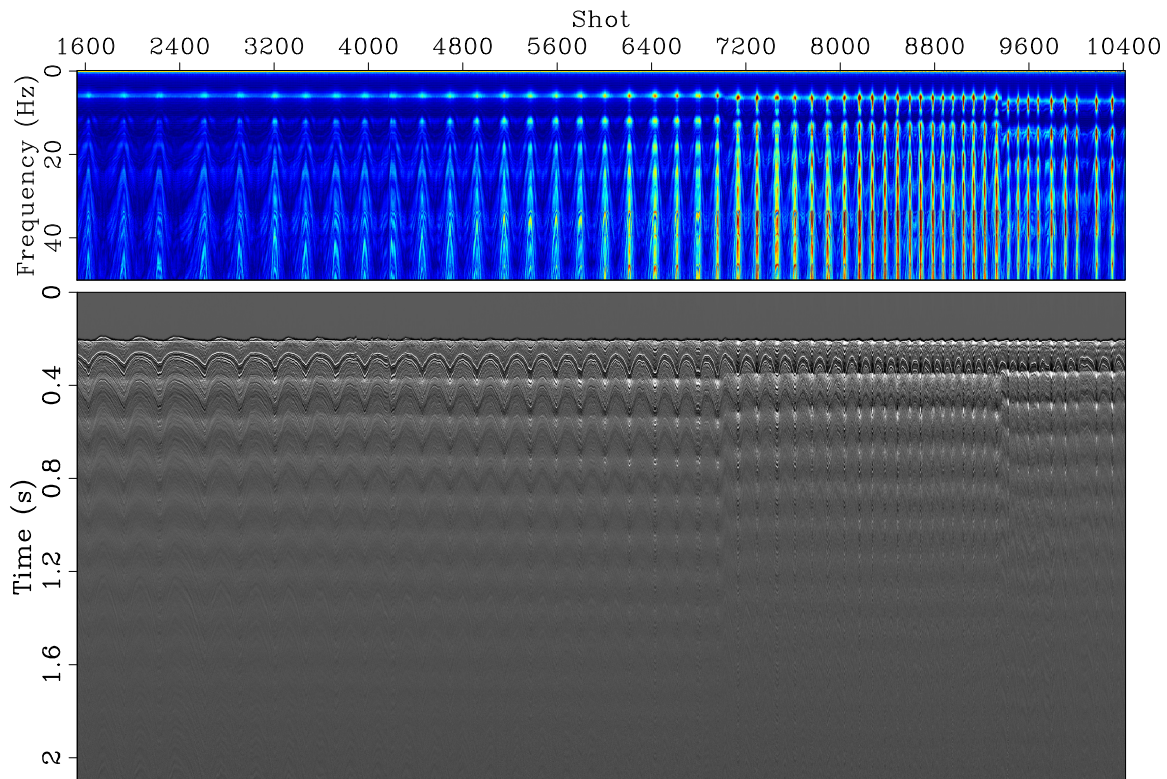


Figure 11: HMO applied to node 002 (bottom) and the spectrum of the data (top). At shot 7000 an airleak started in the airgun causing a loss of pressure. Near shot 9300 an airgun was disconnected causing a loss of volume. Note that with each change, the bubble period decreased and hence the bubble frequency increased causing the apparent lateral discontinuities. [ER] `joseph1/. h-hmo-spec-002, h-hmo-data-002`

To compute the similarity for these data, we needed to extract the three source signatures. To extract these signatures, we performed an alpha-trimmed mean stack (Watt et al., 1983) over all of the traces in each of the zones. The computed source signatures are shown in Figure 12. In comparing the three signatures we observe that these signatures are noisy and we needed a more sophisticated method for extracting cleaner signatures. We also observe that while each of the sources differed in the bubble frequency, they were not that dissimilar. Regardless of these potential issues, we cross-correlated each of these sources with the data shown in Figure 11. We then picked the maximum of each cross-correlation and normalized it by the autocorrelations of the data and the source as shown in Equation (2), thereby giving us the similarity. The similarity sorted by increasing offset is shown in Figure 13 for source one, source two and source three.

## INCORPORATING THE PROBABILITIES INTO INVERSION SCHEMES

We would like to improve current simultaneous source separation inversion schemes using the probabilities that we obtained from computing the radially and similarity

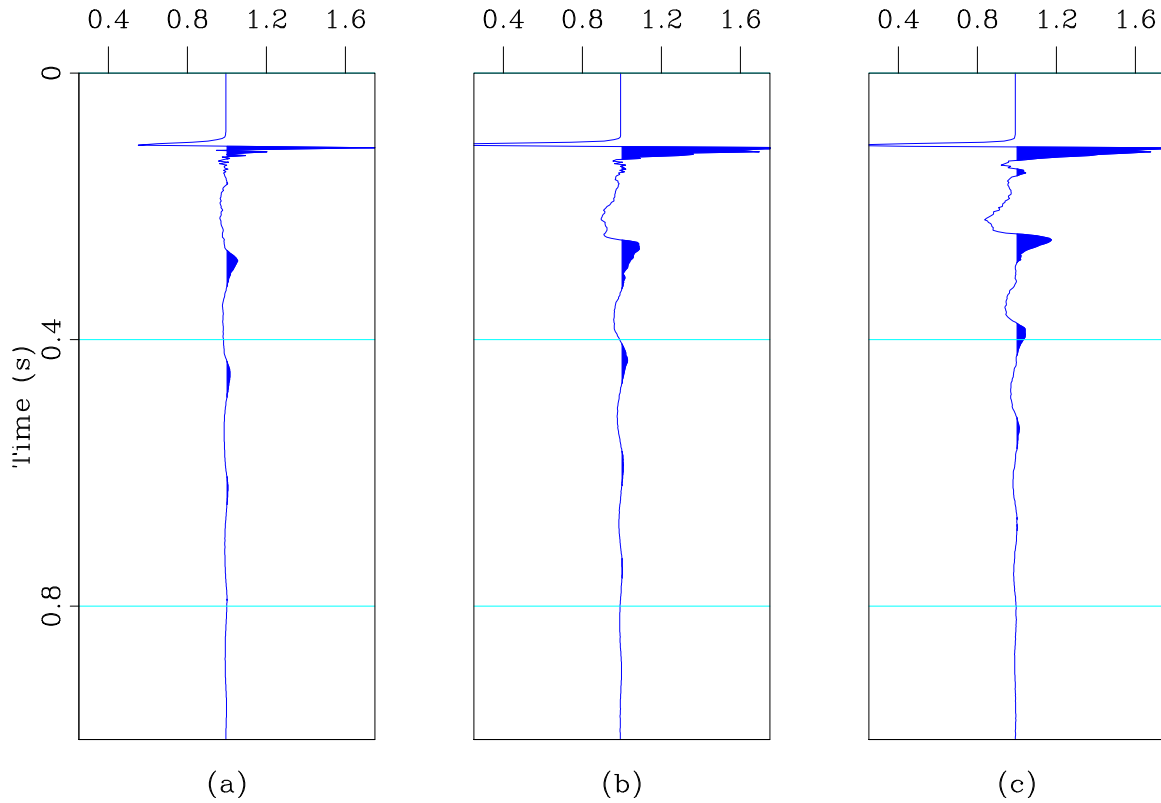


Figure 12: Source signatures from the Forties survey. (a) Signature used over zone one, (b) signature used over zone two, and (c) signature used over zone three. The signature from zone 1 has the longest bubble period and therefore lower frequency content. As the node was placed in zone two (Figure 13(a)), the source from this zone has the most energy. Zone three was acquired using only two airguns resulting in a lower volume therefore giving it the shortest bubble period and highest frequency. **[ER]**

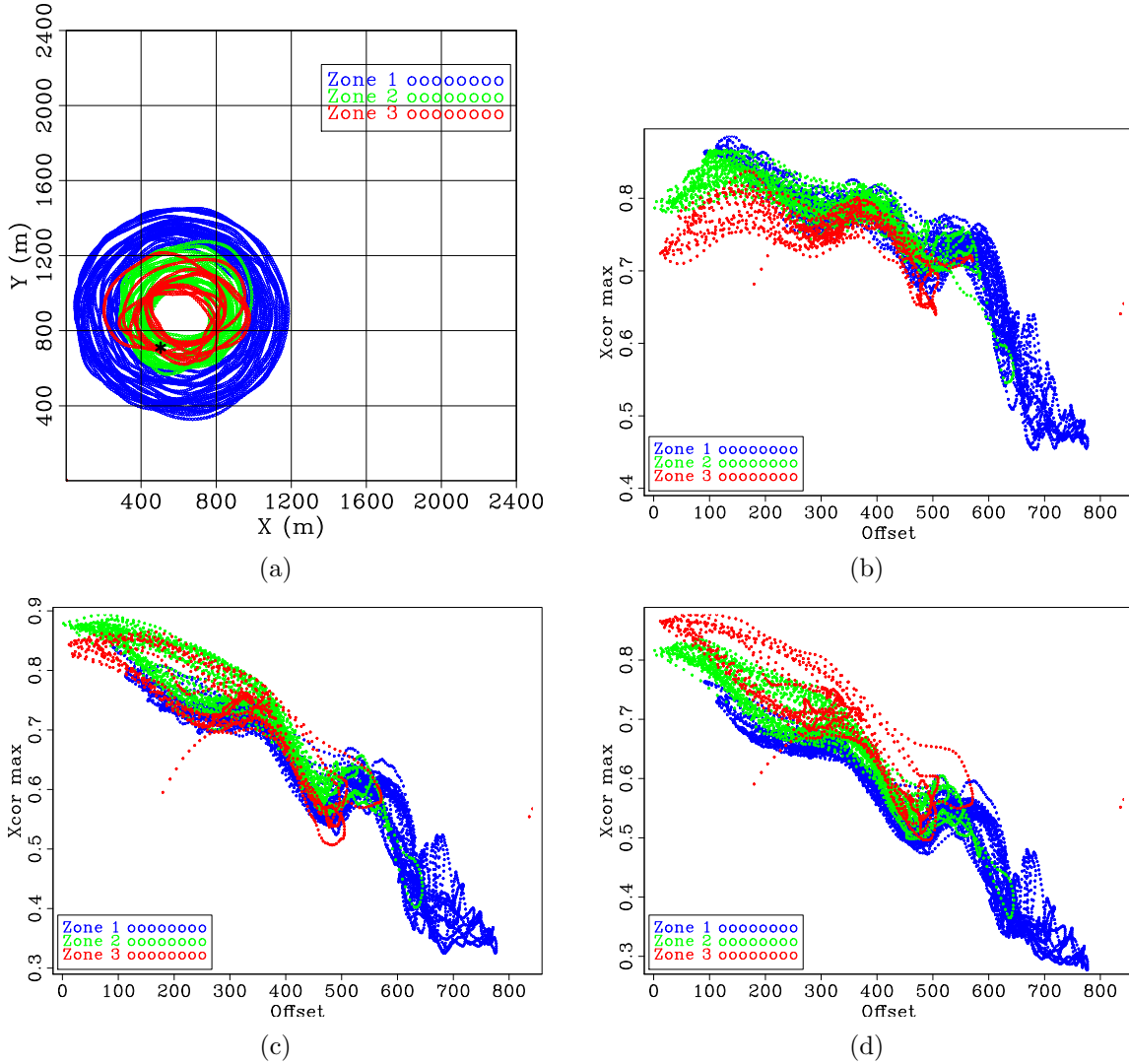


Figure 13: (a) The shot point regions for which the data were acquired with source one (blue), source two (green), and source three (red). The black star indicates the position of the node. (b) The maxima of source one cross-correlated with zones one, two and three, (b) the maxima of source two cross-correlated with zones one, two and three, and (c) the maxima of source three cross-correlated with zones one, two and three. In each of the figures, we expect to see the largest similarity values come from the cross correlations of source one with zone one, source two with zone two and source three with zone three. [ER]

attributes. In the following section, we show a very simple visual example of how this can be achieved. This example shows how incorporating probabilities changes the shape of the objective function for a single parameter estimation problem.

For this example, we desire to minimize the following objective function:

$$J_k(x, y) = -\frac{x^4 + y^4}{(x^2 + y^2)^2}, \quad (3)$$

subject to the following linear constraint:

$$x + y = 2. \quad (4)$$

We also know a priori that the probability that  $x$  is larger than  $y$  is 0.6. Equation (3) is known as the zero-mean kurtosis of a signal and is commonly used as an objective function in geophysics for obtaining sparse solutions to inverse problems (Larue et al., 2005). Combining Equations (3) and (4), we obtain the following univariate objective function:

$$J_k(x) = -\frac{x^4 + (2 - x)^4}{(x^2 + (2 - x)^2)^2}. \quad (5)$$

The plot of Equation (5) is shown in Figure 14(a). Observing this figure, it is clear that there exist two solutions that that minimize  $J_k(x)$ . In order to remove this ambiguity, we can use our additional constraint that we know with 60% certainty that  $x$  is larger than  $y$ . As an objective function, we can write this as

$$J_p(x, y) = (p_x x)^2 + (p_y y)^2, \quad (6)$$

also subject to the linear constraint shown in Equation (4). For this objective function, we desire to minimize  $J_p(x, y)$  and  $p_x$  and  $p_y$  are the certainties to which we know  $x$  and  $y$  respectively. Intuitively, this objective function penalizes improbable models. As  $p_x$  and  $p_y$  are relative probabilities, we can express these as

$$\begin{aligned} p_x &= 0.4, \\ p_y &= 1 - p_x, \\ 0 &\leq p_x \leq 1, \\ 0 &\leq p_y \leq 1. \end{aligned}$$

As before, we combine Equations (6) and (4) resulting in the following univariate objective function:

$$J_p(x) = (p_x x)^2 + (p_y(2 - x))^2. \quad (7)$$

This objective function plotted as a function of the model parameter  $x$  is shown in Figure 14(b). In this figure, it appears that the minimum is close to 1.3. We can then combine  $J_k$  and  $J_p$  into a single objective function  $J_c$  in the following manner:

$$J_c(x) = J_p(x) + \beta J_k(x), \quad (8)$$

where we desire to minimize  $J_c(x)$  and  $\beta$  is a parameter that controls the contribution of the  $J_k(x)$  term in the optimization. The plot of  $J_c(x)$  is shown in Figure 14(c). For this  $J_c(x)$ , we let  $\beta = 4$ . It is clear that the global minimum is very near  $x = 2$ , which according to our initial constraints, is the best model. Using these a priori probabilities, we are able to remove ambiguities in the objective function and arrive at the desired solution.

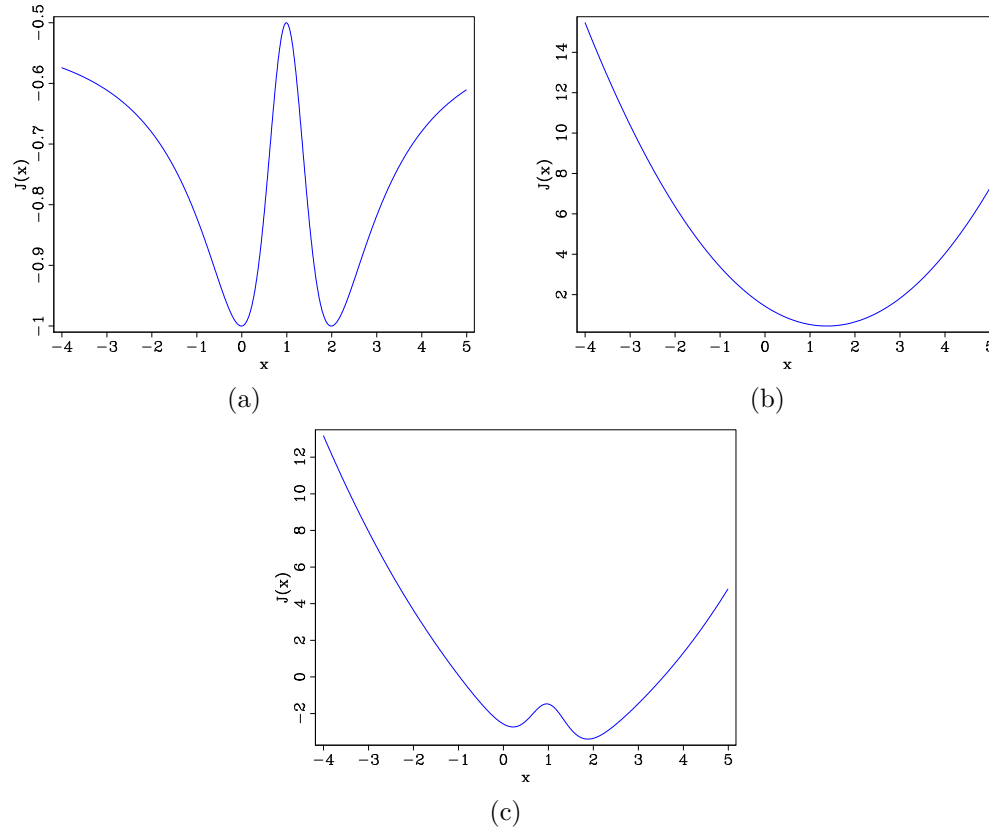


Figure 14: Visual deblending example. (a) The objective function  $J_k$  plotted as a function of the model parameter  $x$ . (b) The objective function  $J_p$  plotted as a function of the model parameter  $x$ . (c) The objective function  $J_c$  plotted as a function of the model parameter  $x$ . [ER]

## CONCLUSION AND FUTURE WORK

In this report, we have introduced two novel attributes that we call radially and source signature similarity that we propose to use in simultaneous source separation inversion schemes. We have demonstrated the computation of these attributes on a node taken from the delta gather of the Apache Forties dataset. We have also presented two toy problems in which relative probabilities were used to improve inversion schemes.

For our future work, we plan to blend the Apache Forties data and subsequently compute the radially and source signature similarity attributes on these blended data. We can then use these attributes as additional constraints in current simultaneous source separation inversion schemes to deblend the blended Apache Forties data.

## ACKNOWLEDGEMENTS

The authors would like to thank Apache North Sea Limited for access to the data set and permission to publish. They also thank the Forties processing summer group for the processing of the raw data and Jason Chang for SEPlib tips. Finally, the authors thank the sponsors of the Stanford Exploration Project for their financial support.

## REFERENCES

- Abma, R. and J. Yan, 2009, Separating simultaneous sources by inversion: 71st EAGE Conference and Exhibition Abstracts.
- Abma, R., Q. Zhang, A. Arogunmati, G. Beaudoin, et al., 2012, An overview of BP's marine independent simultaneous source field trials: 82nd Ann. Int. Mtg, SEG.
- Alves, G., 2015, Overview of the apache forties data set: SEP-Report, **160**, 175–180.
- Beasley, C. J., R. E. Chambers, Z. Jiang, et al., 1998, A new look at simultaneous sources: SEG Technical Program Expanded Abstracts, 133–135.
- Berkhout, A. J., 2008, Changing the mindset in seismic data acquisition: The Leading Edge, **27**, 924–938.
- Chen, Y., 2014, Deblending using a space-varying median filter: Exploration Geophysics, doi:<http://dx.doi.org/10.1071/EG14051>.
- Claerbout, J., 2014, Geophysical image estimation by example: Lulu. com.
- Gaiser, J. E. et al., 1998, Compensating OBC data for variations in geophone coupling: Presented at the 1998 SEG Annual Meeting.
- Huo, S., Y. Luo, and P. G. Kelamis, 2012, Simultaneous sources separation via multidirectional vector-median filtering: Geophysics, **77**, V123–V131.
- Jennings, J. and S. Ronen, 2015, Using Mie scattering theory to debubble seismic airguns: SEP-Report, **160**, 115–130.
- Larue, A., M. Van Der Baan, J. Mars, C. Jutten, et al., 2005, Sparsity or whiteness: what criterion to use for blind deconvolution of seismic data: SEG Technical Program Expanded Abstracts, 1642–1645.
- Leader, C., 2015, The separation and imaging of continuously recorded seismic data: PhD thesis, Stanford University.
- Lynn, W., M. Doyle, K. Larner, and R. Marschall, 1987, Experimental investigation of interference from other seismic crews: Geophysics, **52**, no. 11.
- Ronen, S., A. Kandilarov, C. Massacand, B. Mattocks, J. Paillet, G. Roger, and A. Rokkan, 2012, Onboard data quality control and processing for ocean-bottom nodes: The Leading Edge, **31**, 1168–1176.

- Tang, Y., B. Biondi, et al., 2009, Least-squares migration/inversion of blended data: Presented at the 2009 SEG Annual Meeting.
- Watt, T., J. Bednar, et al., 1983, Role of the alpha-trimmed mean in combining and analyzing seismic common-depth-point gathers: Presented at the 1983 SEG Annual Meeting.
- White, R., 1980, Partial coherence matching of synthetic seismograms with seismic traces: *Geophysical Prospecting*, **28**, 333–358.
- Womack, J., J. Cruz, H. Rigdon, and G. Hoover, 1990, Encoding techniques for multiple source point seismic data acquisition: *Geophysics*, **55**, no. 10.